Assessment of the Vortex Particle-Mesh Method for Efficient LES of Hovering Rotors and their Wakes

Denis-Gabriel Caprace*, Grégoire Winckelmans† and Philippe Chatelain‡.
Université catholique de Louvain, 1348 Louvain-la-Neuve, Belgium

Midway between a vortex method and a grid-based CFD, the Vortex Particle–Mesh method with Immersed Lifting Lines is intended to provide medium-fidelity results on rotor loadings, together with a realistic representation of the 3-D vortical wakes and their dynamics over long distances. We assess the potential of this hybrid approach for the Large-Eddy Simulation of helicopter rotors in hover. A novel Poisson solver with mixed unbounded-outflow boundary conditions here further enables the computation of turbulent hovering scenarios in tight domains. Considering the Knight and Hefner experiment and the S-76 test case as references, we present and compare blade integrated and distributed loads, induction velocities, and wake characteristics. While the quality of the performance predictions highly depends on external polar data, the obtained wakes exhibit similar characteristics to those recently identified in other CFD analyses, here at a moderate computational cost. Based on these results, we further investigate the secondary vortex structures forming between the main tip vortices, and we bring additional clues on their relation to the phenomenon of wake breakdown. We finally discuss the strengths and difficulties of hybrid vortex methods for the challenging analysis of hovering rotors.

I. Nomenclature

α	=	angle of attack
$c, \bar{c}$	=	local chord and mean aerodynamic chord length
$C_t = \frac{t}{\frac{1}{2}\rho(\Omega r)^2 c}$	=	sectional thrust coefficient of a single blade element
$C_T = \frac{T}{\rho(\Omega R)^2 \mathcal{S}}$	=	rotor thrust coefficient
$C_q = \frac{q}{\frac{1}{2}\rho(\Omega r)^2 c R}$	=	sectional torque coefficient of a single blade element
$C_Q = \frac{Q}{\rho(\Omega R)^2 \mathcal{S} R}$	=	rotor torque coefficient
D	=	rotor diameter
$\hat{\mathbf{e}}_x, \hat{\mathbf{e}}_y, \hat{\mathbf{e}}_z$	=	unit vectors defining an orthonormal frame
$FM = \frac{C_T^{3/2}}{\sqrt{2}\, C_Q}$	=	figure of merit
h	=	computational mesh size
N_b	=	number of blades
Q	=	torque of the rotor
R	=	rotor radius
ρ	=	fluid density
s	=	rotor solidity
σ	=	blade mollification parameter
$\mathcal{S} = \pi R^2$	=	reference surface of the rotor
T	=	thrust of the rotor
θ_0	=	collective pitch angle
$\mathbf{u}$	=	local velocity
$\mathbf{x}$	=	spatial coordinate
ω	=	local vorticity
Ω	=	rotor angular velocity

*F.R.S.–FNRS Research Fellow, Institute of Mechanics, Materials and Civil Engineering (iMMC); denis-gabriel.caprace@uclouvain.be.
†Full professor, iMMC; gregoire.winckelmans@uclouvain.be. Senior Member AIAA.
‡Professor, iMMC; philippe.chatelain@uclouvain.be.

II. Introduction

The accurate prediction of the performance of a rotor in hover is critical in the design of helicopters as it overwhelmingly drives the power requirements for the vehicle. In hover, the rotor must indeed guarantee the thrust production while evolving solely within its own induction, i.e. without benefiting from being fed an upstream uniform flow. This results in a high induced power consumed by the rotor.

Despite the overall increase in computational power over the last decades, the simulation of hovering rotors still represents a challenge today [1]. Affordable design tools (including free-wake methods) offer often limited accuracy [2], while detailed predictions are only accessible through very large CFD simulations requiring a huge amount of resources (see e.g. [3] for a recent one). Among quite accurate approaches, the detached-eddy simulation with adaptive mesh resolution effectively captures the near wake of hovering and advancing rotors [4, 5], at the cost of tremendously high resolution simulations with fine body-fitted meshes. A coarser (hence computationally cheaper) but effective representation of the rotor consists in replacing the blades by an equivalent body force immersed in the volume. This technique, which was rarely applied to rotorcraft configurations (see e.g. [6, 7]), is much more popular in the wind energy community for the simulation of wind turbine wakes, where it is known as the Actuator Line Model (ALM) [8–10]. Other CFD methods may use the vorticity-velocity form of the Navier-Stokes equation, like the Vorticity Transport Model (VTM) by Brown *et al.* [11], later also adapted in [12] leading to remarkably accurate results. On the other hand, fully Lagrangian solvers were employed for the simulation of rotors, with a blade representation using either lifting lines [13] or panel methods [14]. Domain decompositions were also developed so as to couple an Eulerian solver for the near body flow computation, and a vortex particle method (or equivalent) in the far field [15–17]. These techniques were developed almost exclusively to provide medium to high quality predictions of the rotor loads. However, they offer various degrees of fidelity regarding the rotor wake, especially in regions far from the rotor.

With the present work, we aim to explore the potential for hover predictions of an original hybrid simulation technique, which recently stood out for the simulation of wind turbine wakes [18–20], and of forward flying helicopter wakes [21], over unprecedented downstream distances (see Fig. 1 as an illustration). The numerical tool is based on a state-of-the-art Vortex Particle–Mesh (VPM) flow solver which combines the advantages of particle and grid-based methods. The originality of the approach relies on its mixed Lagrangian-Eulerian character, guaranteeing low dissipation and dispersion errors, and achieving a high computational efficiency at the same time. The VPM method has benefited from significant improvements over the last two decades, further enabling its Large-Eddy Simulation (LES) capabilities. Immersed Lifting Lines (ILL) were added to model the effect of wings or blades on the fluid.

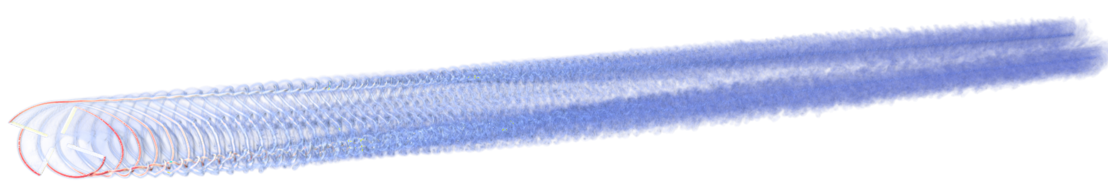

Figure 1 Large-Eddy Simulation of the wake of an advancing helicopter rotor over 30 rotor diameters, using the VPM method (results from [21])

For the present case of hovering, we aim to evaluate the ability of the VPM method with ILL to predict the performance of a hovering rotor, and to obtain an accurate and comprehensive description of its wake. To this end, a novel Poisson solver is introduced to guarantee the proper rotor induction in free-space through the definition of mixed unbounded-outflow boundary conditions. Our simulations then capture the vortex sheets and tip vortices in the near wake, the associated vortex interactions and instabilities, and the transition to a turbulent jet. Concerning the latter, we pay special attention to the phenomenon of wake breakdown and the factors that may affect it, as its significance in numerical simulations is currently questioned in the community [22].

In this paper, we first briefly review the VPM method and the associated modeling techniques (Section III). Opening the results sections, we compare our simulation outputs to the experimental data by Knight and Hefner [23] in Section IV: we assess the overall performance based on the thrust coefficient and on the figure of merit, and we characterize the rotor induction. In Section V, we further compare the load distributions obtained on the S-76 rotor with reference experimental and numerical results. Then, in Section VI, we focus on the wake of both rotors. We emphasize specific flow features that our simulations capture, and we comment on the observed phenomenon of wake breakdown. Finally, we conclude on the benefits and on the challenges of the use of the VPM method with ILL for rotorcraft applications.

III. Numerical method

A. Flow solver

The VPM method relies on the vorticity–velocity ($\boldsymbol{\omega}$–$\mathbf{u}$) formulation of the Navier-Stokes equations for incompressible flows ($\nabla \cdot \mathbf{u} = 0$),

$$\frac{D\boldsymbol{\omega}}{Dt} = (\nabla \mathbf{u}) \cdot \boldsymbol{\omega} + \nu \nabla^2 \boldsymbol{\omega} + \nabla \cdot \mathbf{T}^M , \tag{1}$$

where $\frac{D}{Dt} = \frac{\partial}{\partial t} + \mathbf{u} \cdot \nabla$ denotes the Lagrangian derivative, ν is the kinematic viscosity, and $\mathbf{T}^M$ the sub-grid scales (SGS) model. The velocity field is decomposed as $\mathbf{u} = \mathbf{U}_\infty + \mathbf{u}_\omega$, and $\mathbf{u}_\omega$ is recovered from the vorticity field through the resolution of the Poisson equation

$$\nabla^2 \mathbf{u}_\omega = -\nabla \times \boldsymbol{\omega} \ . \tag{2}$$

We provide more details on how the latter equation is solved in the next section.

The flow is discretized using a set of Lagrangian particles characterized by a position $\mathbf{x}_p$, a volume V_p and a strength $\boldsymbol{\alpha}_p = \int_{V_p} \boldsymbol{\omega} \, d\mathbf{x}$. The evolution of their position and strength is recovered from the resolution of the following ODEs,

$$\frac{d\mathbf{x}_p}{dt} = \mathbf{u}(\mathbf{x}_p) , \tag{3}$$

$$\frac{d\boldsymbol{\alpha}_p}{dt} = \int_{V_p} \Big((\boldsymbol{\omega} \cdot \nabla)\mathbf{u} + \nu \nabla^2 \boldsymbol{\omega} + \nabla \cdot \mathbf{T}^M \Big) \, d\mathbf{x} , \tag{4}$$

which are here integrated using a third order Runge-Kutta scheme. The spatial differential operators (right-hand-side of Eq. (4)) are evaluated using finite differences computed on an underlying Eulerian grid, and mid-point quadrature for the integrals. The turbulence SGS model ($\nabla \cdot \mathbf{T}^M$) also uses the grid and is implemented as in [24]. High order interpolation schemes are used to recover information back and forth between the particles and the mesh. Other improvements of the VPM method include the periodic operations of remeshing and reprojection. The former prevents particles to deplete some regions of the flow or cluster in others, while the latter maintain the solenoidal property of the vorticity field, which is otherwise not directly enforced by the solver. We refer to the prominent reviews by Cottet and Koumoutsakos [25] and by Winckelmans [26] for further details on the VPM method and on the theoretical background. Additionally, Chatelain et al. [27] provide a thorough description of the present implementation on massively parallel architectures (here based on the open-source PPM library [28]). Overall, this hybrid framework provides low dispersion and dissipation errors, and also waives the classical CFL condition, thus allowing for large time steps.

B. Poisson solver and unbounded boundary conditions

The Poisson solver computes the solution of Eq. (2) on the underlying uniform Cartesian grid with specified boundary conditions. For performance reasons, the solver operates in Fourier space, and the related numerical technique (which maintains second order in space) benefits from a very efficient 3-D fast Fourier transform algorithm. Originally implemented by Chatelain and Koumoutsakos [29], the solver was recently enhanced and refactored into a dedicated software library called *FLUPS* [30]. Importantly, it now accommodates the simultaneous definition of any combination of periodic, unbounded, semi-unbounded, inlet and outlet boundaries.

For the present simulations of hovering rotors, we impose free-space conditions on 5 of the 6 boundaries of the computational domain. For the last one (the bottom one), an outflow condition is obtained by imposing symmetries on $\mathbf{u}_\omega$, and correspondingly on $\boldsymbol{\omega}$. For instance, we assume an odd parity of the vorticity component normal to the boundary, and an even parity for the tangential components. Consequently, the essentially tangential vorticity in the wake jet can easily connect to the outflow plane, hence providing a clean outflow. On all the other unbounded boundaries, the streamlines of the flow can connect to the infinite outer domain with no prescribed direction or path (as opposed to what the symmetric condition does), guaranteeing no blockage effects or forced/wrong induction. Correct unbounded results are thus obtained on computational domains which tightly enclose the vorticity.

C. Blade model using Immersed Lifting Lines

The rotor blade coarse scale aerodynamics are accounted for through an Immersed Lifting Line (ILL) method [18], recently validated and improved [31]. This technique presents strong similarities with the ALM, except that it is fully compatible with the Lagrangian character of the VPM method. The ILL readily takes care of the generation of vorticity, instead of applying a force in a volume. Based on the instantaneous velocity and angle of attack of every blade segment, the lift and drag produced by the airfoil are retrieved from tabulated aerodynamic polars. Then, under the assumption of quasi-steady flow around the airfoil, the circulation around the local 2-D airfoil is recovered from

$$\boldsymbol{\ell} = \rho \mathbf{U}_{\mathrm{rel}} \times \boldsymbol{\Gamma} \,, \tag{5}$$

where $\boldsymbol{\ell}$ is the lift per unit span of the segment, $\mathbf{U}_{\mathrm{rel}}$ is the relative flow velocity and $\boldsymbol{\Gamma}$ is the circulation vector (along the blade span). In the flow, the blade segments are then represented by a set of equivalent bound vorticity particles, accounting for a spatial mollification required for numerical purposes. This mollification corresponds to a Gaussian spreading (of mollification parameter σ) that covers a few mesh sizes h, in the direction of $\boldsymbol{\ell}$. The shed vorticity, which is deduced from the time and space variations of the bound vorticity, is released in the bulk flow through new vorticity-carrying particles (also with mollification) and then merged with the pre-existing flow particles.

Considering the sharp rectangular shape of rotor blades, we explicitly introduce a numerical smoothing of the tip. In practice, the blade chord is brought to 0 over two computational cells, thus slightly modifying the chord distribution with a length c at $R - h$, $c/2$ at R, and 0 at $R + h$; where h is the mesh size. This helps mitigate the effect of the mollified vorticity field (and the consequence on the measured downwash/induction), which otherwise gives rise to spuriously high loads at the very tip of the blade [32, 33].

D. Rotor hub model

The rotor hub is accounted for through a penalization of the Navier-Stokes equations *à la* Brinkman [34]. The primary purpose of this model is essentially to capture the blockage effect associated with the rotor hub, assimilated to a solid sphere. For simplicity, we implement the explicit version which, in the vorticity-velocity formulation, amounts to complementing Eq. (1) with the term

$$+\,\frac{1}{\tau}\nabla \wedge \left(\chi(\mathbf{u}_s - \mathbf{u})\right), \tag{6}$$

where χ is a mask function equal to 1 inside the solid body and 0 outside, $\mathbf{u}_s = \mathbf{0}$ is the velocity inside the body, and $\tau = \lambda dt$ is a wisely chosen time scale (mainly constrained by stability). We chose to work with $\lambda = 1$, and with a regularized mask function,

$$\chi(r) = \frac{1}{2}\left(1 - \mathrm{erf}\left(\frac{r - R_h}{h}\right)\right), \tag{7}$$

where r is the radius from the hub center, R_h is the assimilated rotor hub radius and h is the uniform spatial resolution of the VPM method.

IV. Results on the Knight and Hefner rotor

A. Rotor configuration

We reproduce numerically the experimental setup by Knight and Hefner [23] who studied several rotor geometries with various solidities. We focus on the 3-blade configuration, the properties of which are summarized in Table 1. The rotor solidity is defined as $s = \frac{\bar{c}\,N_b}{\pi\,R}$. The blades have a constant chord $c = \bar{c}$, and are assumed rigid, untwisted and unswept. We use the polar data provided in the same reference for the NACA0015 (without dynamic stall modeling), experimentally obtained at Re = 2.42 10^5.

Table 1 Rotor and blade characteristics of the Knight and Hefner experiment.

Rotor angular velocity, Ω $[RPM]$	960
Rotor radius, R $[m]$	0.762
Blade chord, c $[m]$	0.0508
Solidity, s	0.0637
Airfoil	NACA0015
Root cut-out, R_i $[\%R]$	16.7%
Rotor hub, R_h $[\%R]$	3.3%

We compare the rotor performances predicted by our numerical setup with the experimental data, for several values of the collective pitch angle θ_0. The blade dynamics are prescribed with a coning angle of 0° (i.e. flapping is neglected).

The effect of the rotor hub is accounted for through the penalization technique described in the previous section. This was necessary to avoid an unsteady effect of the starting flow. When the rotor is impulsively started in a quiescent domain, a large vortex ring forms in the outboard region by the merging of initial tip vortices. This vortex ring advects downwards due to its self-induced velocity. However, a similar mechanism allows root vortices to generate a smaller vortex ring to form in the inboard region, that travels upwards. When present, this structure soon reaches the domain boundary (which can be as close as $D/2$ above the rotor) and would require the domain to grow. The addition of a hub, even if coarsely resolved, introduces a blockage effect near the rotor axis which perturbs the formation of the root vortex ring. The result is a weaker vortex that is hence no longer able to reach the domain boundary, and is progressively absorbed through the rotor. As will be shown hereafter, the root region can still experience a reverse flow in steady condition, which is associated with a vortex ring attached to the rotor.

Three resolutions are used for the simulations: a coarse level with 64 particles per D (i.e. $\frac{h}{D} = 64$), a medium level with 128 particles per D, and a fine level with 192 particles per D. The time to solution for the finest grid is of the order of 12 hours on 216 CPUs. The presented results are time-averaged over eight rotor revolutions.

B. Rotor performance

Figure 2a presents the thrust coefficient where the thrust is measured along the rotor shaft. Even though the blades are modeled with ILLs, we stress that the drag of each blade section is well taken into account when computing the forces and torques. The figure of merit is shown in Fig. 2b.

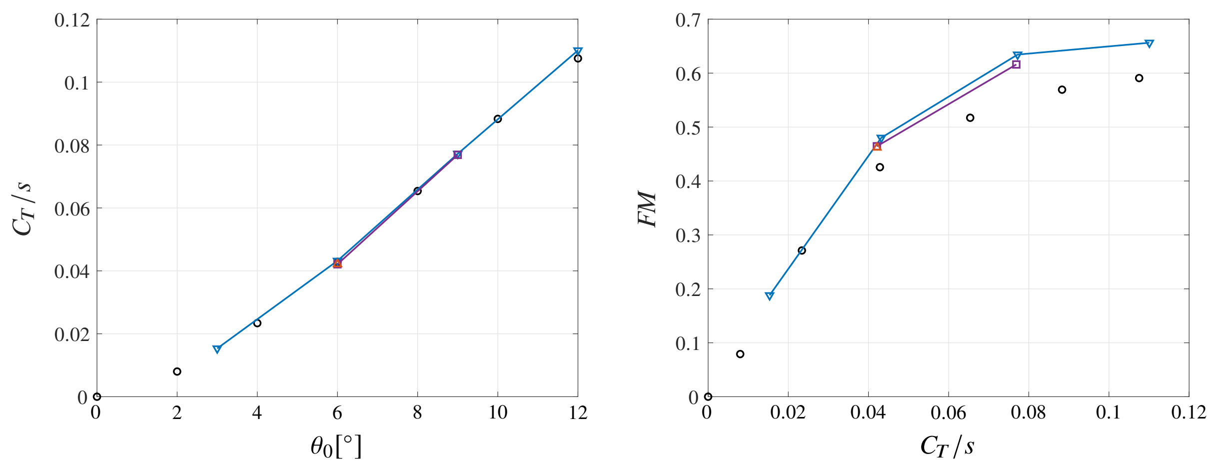

(a) Thrust coefficient over solidity

(b) Figure of merit

Figure 2 Results on the Knight and Hefner experiment (○), VPM coarse (▽), VPM medium (□) and VPM fine (△).

A good agreement is obtained for the thrust coefficient with our numerical method. However, the figure of merit is over-predicted. This behavior could be expected from previous results on other rotary configurations such as wind turbines [18, 20], where the ILL systematically predicts higher tangential loads. Consistently, a similar trend is generally observed with the actuator line model, as reported in [33, 35] (among others). The origin of this discrepancy is traced back to a mismatch in the tip loads caused by the mollification inherent to the lines [32]. The induced velocity at the tip of the blades drops, hence increasing the angle of attack in that region. For rotary wings, this results in a slightly higher predicted thrust and a lower torque (due to the tilting of the local lift vector), as confirmed here by the over-predicted FM.

Even though the increase in resolution slightly reduces the discrepancy with the experimental results, the FM here still converges to over-estimated values (almost no change between the medium and high resolution simulations), which indicates the presence of other sources of discrepancy than the mollification. In particular, the use of 2-D airfoil polars

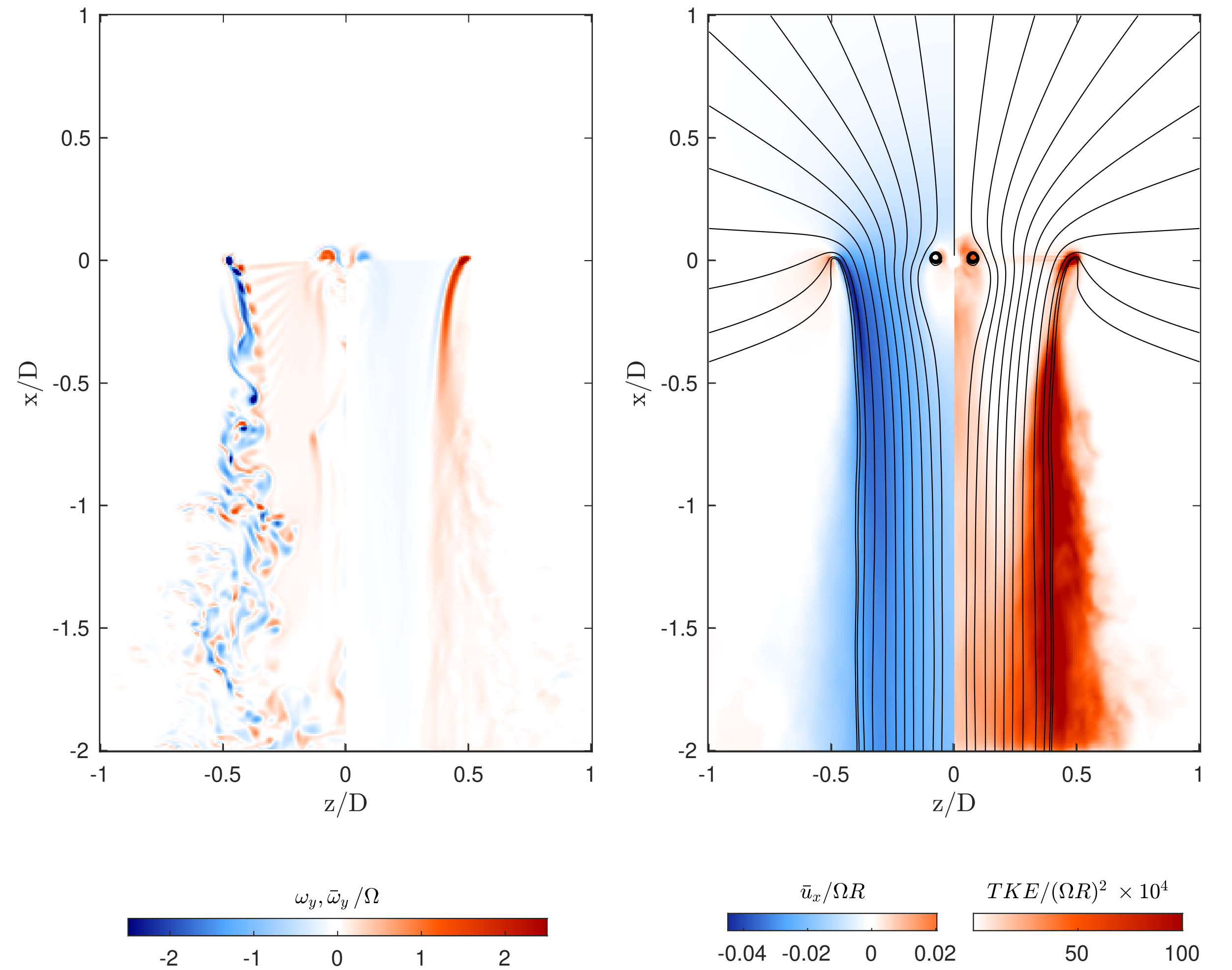

(a) Instantaneous (left half-plane) and mean (right half-plane) tangential vorticity

(b) Axial induction (left half-plane) and turbulent kinetic energy (right half-plane)

Figure 3 Cross-section of the flow through the hovering Knight and Hefner rotor with $\theta_0 = 6°$ and a resolution of 128 particles per diameter. The axes span the full extent of the computational domain.

generally leads to an overprediction of lift and underprediction of friction drag in the near tip region, where 3-D effects become important. Those could be corrected for by appropriately degrading the 2-D polars in the near tip region, and is work in progress. Furthermore, the combined effect of mollification in the ILL and blade-vortex interaction (BVI) can here also contribute to the loss of accuracy in the near tip loads. This hypothesis is discussed in more details in Sections V and VI.

C. Rotor induction

Figure 3 shows the mean flow in a cross-section passing through the center of the rotor. At each passage of the blade observed in Fig. 3a, the vortex shed at the tip is accompanied with a region of opposite-sign vorticity just inboard of that location. The origin of this vorticity will become clear with the analysis of the blade loading. The successive tip vortices merge when they are roughly one revolution old, then forming a vortex sheet. Downstream, this sheet undergoes instabilities about 0.4 D below the rotor, evidenced by the instantaneous field; this corresponds to a spreading effect in the mean. The whole wake then progressively transitions to a turbulent jet further downstream.

Inboard of the rotor, two areas of non-zero vorticity exist above the rotor plane. They are caused by the root vortices indeed shed upwards, which then recirculate through the rotor. On average, this forms a vortex ring attached to the rotor, which is materialized by the streamlines visible in Fig. 3b.

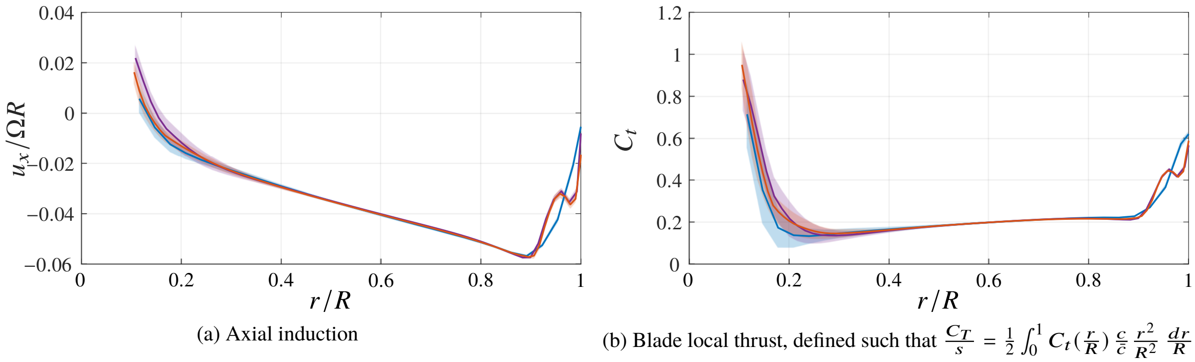

Figure 4 Blade mean spanwise distributions at $\theta_0 = 6°$: coarse (—), medium (—) and fine (—) resolutions. Colored areas represent the 1-standard deviation enveloppe.

Our model of the hub is clearly noticeable as an area of zero velocity and zero turbulent kinetic energy (TKE = $\frac{1}{2}(\overline{u'_x u'_x} + \overline{u'_y u'_y} + \overline{u'_z u'_z})$, where the prime denotes velocity fluctuations), with a stagnation point at the top. In the whole inboard region downstream of the hub, the TKE hints at large velocity fluctuations, even though the mean axial velocity is insignificant in that region. On the other hand, the axial induction is maximum at the tip, and the streamlines show that the flow passing through the rotor is indeed sucked from the entire half-plane above the rotor, and even partially from below the rotor. Even though not documented in the experiment, the wake contraction resulting from the simulation agrees qualitatively well with the expected result.

These results illustrate the ability of our Poisson solver to ensure the unbounded condition required for hovering, on 5 of the 6 boundaries, even in a computational domain enclosing the rotor rather tightly. This constitutes quite an achievement, as we could not find in the literature any other numerical method that allows to do that, despite the high sensitivity of hovering rotor simulation results to the boundary conditions of the problem [1]. In particular, the definition of truly unbounded boundary conditions in any incompressible method based on a conventional velocity-pressure ($\mathbf{u}$–p) formulation is not straightforward. Solutions based on a domain where the unbounded boundary conditions are arbitrarily replaced with other types of BCs are likely inaccurate [36], or require to put the boundaries very far.

Because of the strong contraction of the vein just downstream of the rotor, the interaction between the blade and the tip vortices shed by the preceding one occurs inboard of the tip radius (as opposed to a rotor in a "windmill" state where tip vortices are advected outboard).

Recall that the ILL represents the entire blade as an equivalent bound vortex, located at the quarter chord line. This bound vortex is mollified using a Gaussian regularization (of parameter σ) discretized using several vortex particles in the direction of the local lift vector. The mollification of the blades affects the intensity of this BVI in a non-trivial way.

From experimental and CFD results, it is generally observed that the blade passes above the preceding vortex, with a clearance depending on the rotor loading. However, when the ILL employs high σ/R, the mollified blade may overlap with the resulting smeared vortex, whereas smaller ratios lead to the blade indeed passing above the vortex. Crucially, this BVI is responsible for a strong gradient in the induced velocities measured in the tip region, as shown in Fig. 4a. Hence, the loads are notably increased over a distance spanning between the location of the interaction (here at $r/R \approx 0.9$) and the blade tip, Fig. 4b. With the second test case, we further investigate this BVI and its effect on the ILL behavior.

V. Results on the S-76 rotor

A. Rotor configuration

The S-76 rotor has been extensively studied in recent years as part of the AIAA Rotorcraft Hover Prediction Workshop*. In addition to the original experimental data [37, 38], a common effort from the community has led to numerous numerical studies based on a variety of CFD methods (see the partial summary in [1], then e.g. [3, 5, 39]).

*Test cases from the AIAA Rotorcraft Hover Prediction Workshop are available at `https://aiaahover.wixsite.com` (last accessed November 2020).

Rotor angular velocity, Ω $[RPM]$	1524
Rotor radius, R $[m]$	1.423
Blade chord, c $[m]$	0.0792
Solidity, s	0.0709
Root cut-out, R_i $[\%R]$	18.9%
Rotor hub, R_h $[\%R]$	8.3%

Table 2 S-76 rotor and rectangular blade characteristics

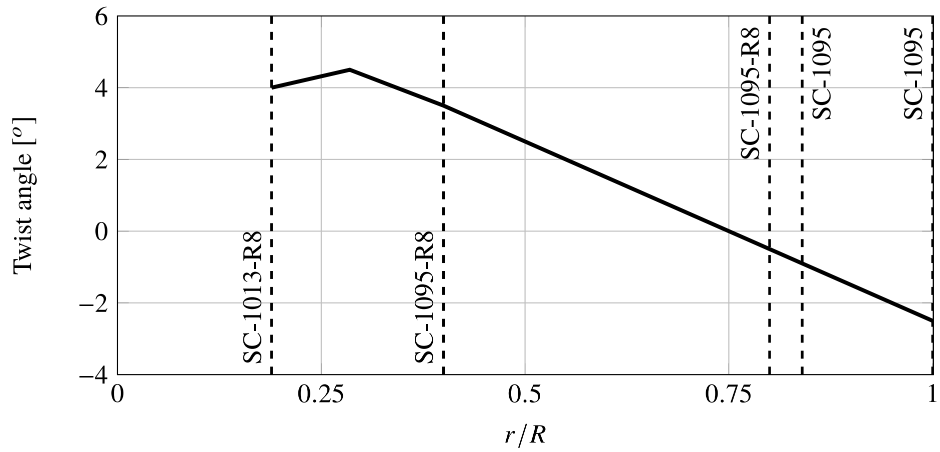

Figure 5 Blade twist distribution and airfoil stations

Starting from the isolated rotor configuration, several sub-cases have been considered including different blade tip geometries (with sweep and anhedral), and various tip Mach numbers.

In this work, we focus on the rectangular tip geometry and we simulate the case corresponding to a tip Mach number of $M_{\text{tip}} = 0.65$. The rotor characteristics are summarized in Table 2. Again, the blades are assumed rigid. The twist distribution follows the workshop definition shown in Fig. 5 and the blades have a constant chord over the entire span ($c = \bar{c}$). In our setup, we again add an arbitrary spherical hub for the same reason as in Section IV.

We use *XFOIL* [40] to obtain airfoil polars corresponding to the average flow conditions of the five spanwise stations defined along the blade (see Fig. 5). The polars, shown in Fig. 6, leverage the capabilities of *XFOIL* to account for viscous and compressibility effects. In the VPM simulations, the local lift and drag coefficients are obtained from a linear interpolation of the polars along the span of the blade.

We simulate the S-76 rotor at the medium and high spatial resolutions (128 and 192 particles per D). The computations are performed in a domain of size $[3R \times 3R \times 3R]$. The rotor is placed at $0.8R$ from the above boundary. The coning angle is prescribed to 2.5°, 3.5° and 4° at a collective pitch of $\theta_0 = 4°, 6°, 8°$ respectively.

B. Rotor performance and loadings

Figure 7 show obtained thrust and torque coefficients, compared to experimental data and numerical results from the literature. The thrust is slightly overpredicted; yet it is still within 5 percent of the experimental data. Compared to the previous test case, this loss of quality is mainly attributed to inaccuracies in the polars. Despite its simplicity of use, the nature of the method (combining vortex panels and integral boundary equations) indeed limits the fidelity of XFOIL predictions. On the other hand, as observed on the Knight and Hefner rotor, the predicted torque is too small, leading to erroneously high FM. This effect cannot be entirely attributed to polar inaccuracies; it is also related to the other effects mentioned in Section IV.B, which we further investigate here. As visible in Fig. 7b, standard CFD methods are typically capable of predicting the figure of merit with less than 5 percent error.

Advantageously, and unlike Knight and Hefner's experiment, loading distributions are well documented for the S-76 rotor. This enables a more in-depth comparison of our results with external references, leading to further insights into

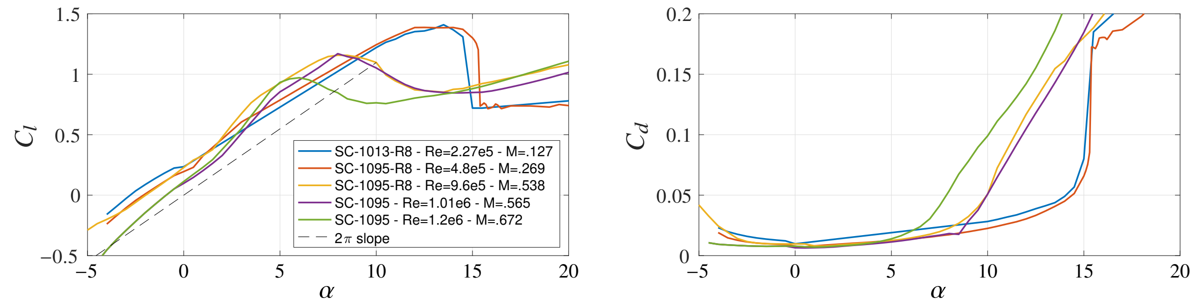

(a) Sectional lift coefficient

(b) Sectional drag coefficient

Figure 6 Airfoil polars corresponding to the average Reynolds and Mach numbers for each airfoil section defined along the blade, generated using XFOIL with $N_{\text{crit}} = 9$.

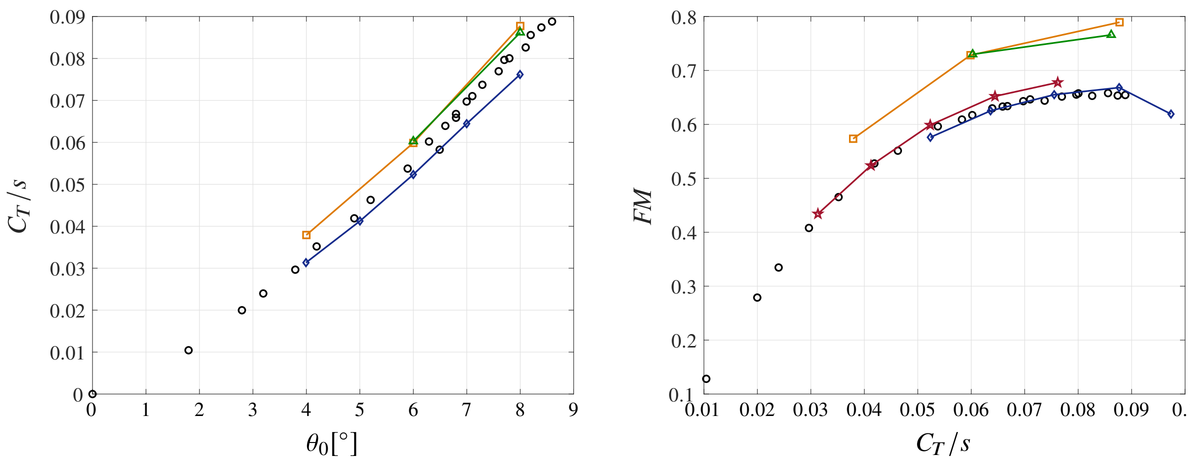

(a) Thrust coefficient over solidity

(b) Figure of merit

Figure 7 Performance of the S-76 rotor: experimental data from [37] (○); CFD results by Garcia and Barakos [41] (◇) and by Jain [5] (☆); VPM results at medium (□) and high (△) resolutions.

the origin of our too small C_Q.

Figure 8 presents the blade thrust and torque distributions compared to a numerical reference. Results compare fairly well between $r/R = 0.3$ and 0.8. In the root region, discrepancies originate in polar inaccuracies and in the influence of the hub which may affect the local flow conditions, hence the angle of attack (AoA). A more fundamental issue can be observed at the tip where large discrepancies exist on both thrust and torque. As previously described, this region is affected by a strong parallel BVI: the preceding tip vortex reaches the blade at approximately $r/R = 0.92$ and induces a modification of the AoA leading to smaller C_t inboard of the location of the interaction, and larger C_t outboard. The reference CFD exhibits the large C_t outboard, but the inboard change seems exaggerated in the VPM simulation. Again, the XFOIL-produced polars contribute to inaccuracies, as we notice a clear discontinuity in the slope of C_t and C_q at $r/R = 0.8$ and 0.85. This region corresponds to a transition between two of the main sections defined in Fig. 5.

As the tip load is crucially dependant on the BVI described above, the accurate capture of the vortex trajectory is thus critical. In the present case, the blade should skim over the preceding tip vortex. However, as explained in Section IV.C, the presence of mollification affects the vortex size and it here results in the vortex partially impinging the blade. In reality, near wake effects and the actual geometry of the tip may also interfere with the formation of the vortex, something that we do not capture here. Furthermore, strong BVI are capable of inducing spanwise flow or triggering flow separation [42]. None of these effects are accounted for in a simple lifting or actuator line model.

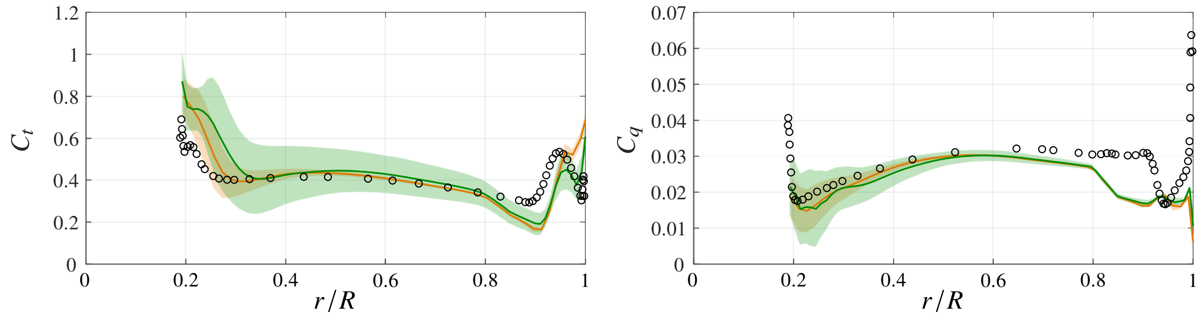

(a) Blade thrust distribution

(b) Blade torque distribution

Figure 8 Spanwise distributions of the blade thrust and torque, comparing VPM results at $\theta_0 = 6°$ with medium (—) and high (—) resolutions; and numerical results by Jain [5] at $C_T/s = 0.064$ (∘). Colored areas represent the 1-standard deviation enveloppe.

To conclude on the use of the ILL in this context, improved quality polars could definitely lead to an increase in the method accuracy for load prediction. Dedicated techniques are currently under investigation to mitigate the effect of the mollification [33, 43], which should also contribute to enhance the level of fidelity. Degrading the polars near the blade tip, so as to better account for 3-D effects, is also being investigated. However, the proper capture of the BVI still poses a significant challenge to lifting and actuator line techniques. It is so far effectively captured only when using blade-resolved CFD.

In fact, because of the absence of forcing through an imposed upstream velocity, the hovering rotor constitutes a problem highly sensitive to blade modeling and computational methodology, even more than conventional wind turbines. The solution results from a delicate equilibrium between the shed vorticity, its dynamics and the intrinsic feedback it has on the modeled aerodynamics of the blade; all these elements being tightly coupled, and strongly dependent on the mollification, the airfoil polars, and on the boundary conditions. Generally, this tight coupling, combined with the need for unbounded boundaries (that we indeed overcame here), contributes to the most challenging aspects of modeling hovering rotors. Configurations with a forcing velocity (such as wind turbines) are more tolerant to modeling and computional variations.

VI. Hovering rotor wakes: coherent vortex structures and wake breakdown

A 3-D vizualization of the vorticity produced by the Knight and Hefner rotor is shown in Fig. 9. Tip vortices remain coherent over approximately one rotor revolution. We notice the presence of secondary, streamwise-aligned vorticity structures entangled between the primary tip vortices. These structures visibly play a major role in disturbing the main tip vortices, eventually contributing to the breakdown of the wake into a fully turbulent jet. This behavior was also observed in several other CFD simulations (see [44] for a summary), although it does not seem to be consistently predicted across various numerical setups. Indeed, the capture of the secondary structures in RANS simulations is highly sensitive to numerical parameters (mesh structure and resolution, turbulence modeling, etc.), which in turn raises question about their physical significance. In fact, the role of the secondary structures in the wake breakdown is listed by Egolf et al. [1] among the most important unanswered questions in modern hovering rotor simulations.

In this section, we aim to bring additional clues on the physical process leading to the appearance of the secondary vortical structures, using our LES-enabled hybrid vortex method.

A. Tip vortices generation and blade-vortex interaction

Similarly to our simulation of the Knight and Hefner rotor, the tip vortices of the S-76 merge into a diffuse vortex sheet when they are approximately one revolution old in our high resolution configuration, and even sooner for the medium resolution (see Fig. 10). This happens way earlier than what is generally observed from high-resolution CFD, and can be explained by our relatively lower resolution. Our tip vortices are correspondingly of a larger size, directly proportional to the mollification parameter σ.

In both test cases, the BVI in the tip region results in additional vorticity being shed from the blade at the location of

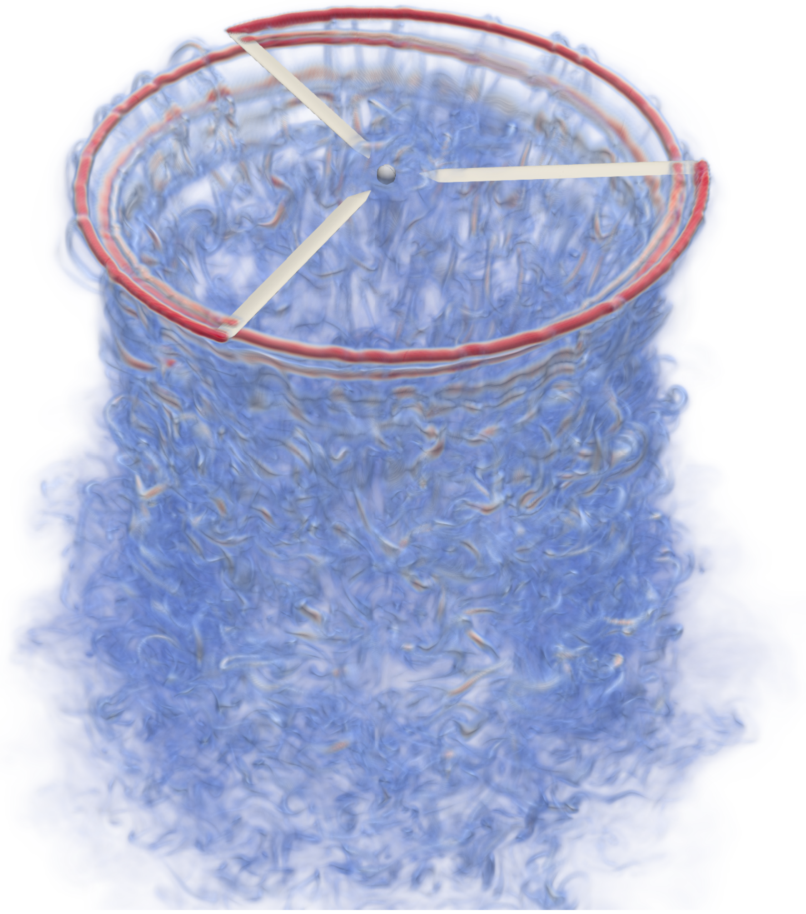

Figure 9 Volume rendering of the vorticity magnitude in the wake of the Knight and Hefner [23] rotor at $\theta_0 = 6°$ (high resolution case, 192 particles per D).

the interaction. Again, this is not observed in high resolution CFD simulations, which confirms that the ILL should be adapted to better handle the BVI. In the current version of the model, this added vorticity is of opposite sign of the main tip vortex, and hence contributes to the tip vortex in a destructive way. After the first BVI indeed, the tip vortex rapidly smears in our medium resolution case. In the high resolution case, an independent small vortex is shed at the location of the interaction and travels along the main tip vortex, later contributing to a mutually induced instability.

Despite these departures from the expected tip vortex structure, the occurence of secondary structures is here notable. These perpendicular vortices appear as entangled between successive tip vortices, following a process that we intend to describe in the next section.

B. Secondary structures and wake breakdown

We focus on the high-resolution simulation of the S-76 rotor at $\theta_0 = 8°$. Figure 11 presents the temporal evolution of the flow over a quarter revolution. Inspecting the relatively clean tip vortex shed from the blade, we observe secondary vortical structures appearing outboard, after approximately the eighth of a revolution. These structure emerge as vortex filaments crawling upstream, and progressively wrap around the main tip vortex. After the passage of the following blade, the transverse filaments eventually end up entangled between two tip vortices, which results in high stretching. Under the effect of the related velocity gradients, the vorticity from the vortex sheet in the wake of the blade aggregates and contributes to the transverse filaments, feeding the process for the subsequent blade passages.

Experimental results recently confirmed the presence of these secondary structures in the wake of a hovering rotor [45]. Akin to what was hypothesized by other authors in the literature, our results support that the secondary filaments originate in the high stretching of the portions of vortex sheets located between two successive tip vortices.

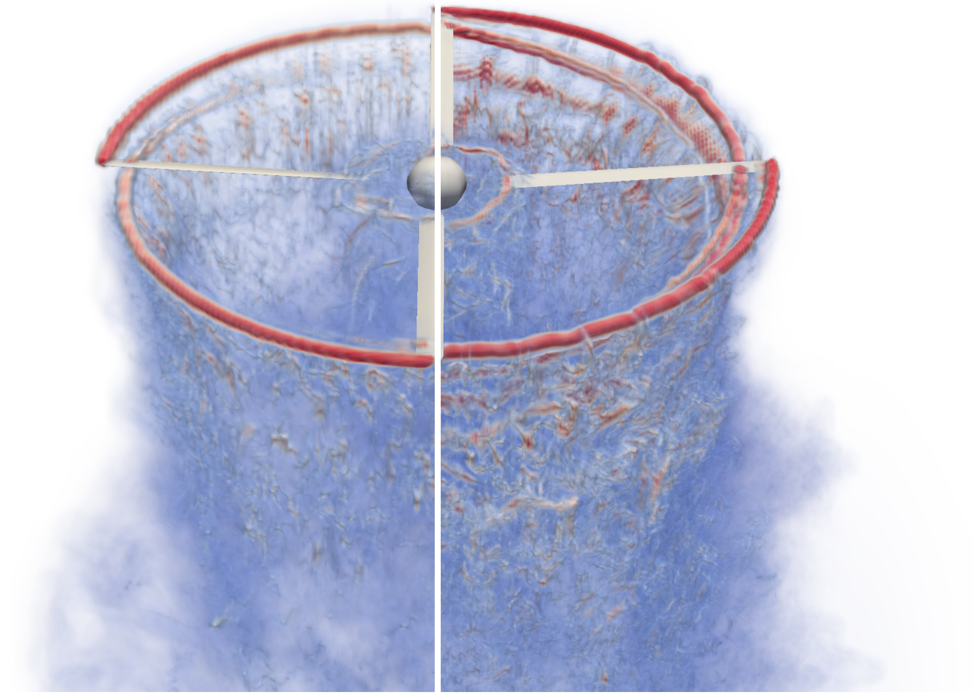

Figure 10 Volume rendering of the vorticity magnitude in the wake of the S-76 rotor at $\theta_0 = 8°$, at medium resolution with 128 particles per D (left), and at high resolution with 192 particles per D (right).

Often, a parallel was made between the secondary structures observed in this context and the streamwise filaments forming between large spanwise vortices in a shear layer. In this type of flows (studied by the authors in [46]), extreme stretching of the initial vortex sheet indeed occurs between the main rollers. Such conditions are favorable to the onset of streamwise-aligned filaments (a.k.a. braids), as can be seen in Fig. 12.

From our simulation, it seems however difficult to identify a spatial organization pattern of these structures. In particular, they appear to be distributed randomly over the rotor revolution. Yet, we notice that the present method captures them at a comparatively affordable resolution, whereas the previously-mentioned CFD methods require a much more resolved setup.

While the existence of the secondary structures in the actual flow makes little doubt, the possibly too large extent of the phenomenon in numerical simulation is disputed, in particular because it can be responsible for an early breakdown of the entire wake. When they age, the main tip vortices are prone to further instabilities as the secondary filaments constitute local perturbations capable of exciting unstable modes of the vortex system. The prediction of the wake breakdown is hence contingent on the accurate description of the primary tip vortices and the secondary entangled filaments.

As summarized by Hariharan [22], the capture of secondary vortices in CFD studies is largely dependent on various numerical factors, including the computational method itself, the mesh configuration and resolution, the turbulence model, etc. In the context of the present hybrid particle–mesh method, the resolution of the Cartesian grid plays an obvious role (no secondary vortices are observed on our medium resolution simulations). Related to the ILL, the mollification parameter is effectively driving the size of the vortices and thus affects the obtained flow features. However, as demonstrated in other applications [20, 21], the use of particles provides here a clear advantage for the advection of the vortices, and the SGS model accommodates the appropriate level of turbulent diffusion.

Still, in our "high" resolution simulation, the wake of the S-76 rotor breaks down when the main tip vortices reach the age of approximately one rotor revolution. Even though no experimental measurements exist to quantify the actual location of the breakdown, it is generally accepted that such an early breakdown is unphysical. Increasing the resolution should help reduce the size of the mollified vortices and better capture small-scale interactions; however, an improvement of the ILL model itself is necessary to better handle the BVI and the resulting shed vorticity.

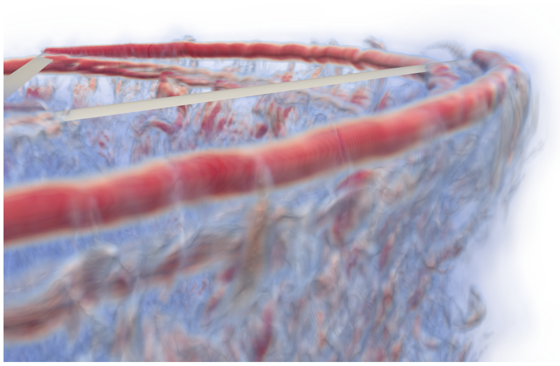

(a) $\frac{t-t_0}{\tau} = 0$

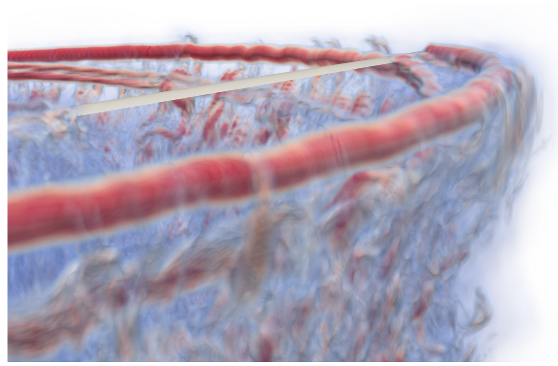

(b) $\frac{t-t_0}{\tau} = \frac{1}{24}$

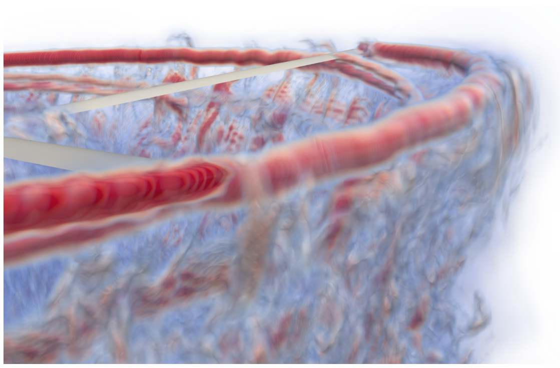

(c) $\frac{t-t_0}{\tau} = \frac{2}{24}$

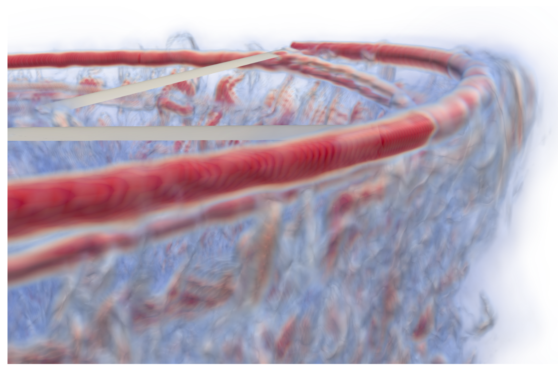

(d) $\frac{t-t_0}{\tau} = \frac{3}{24}$

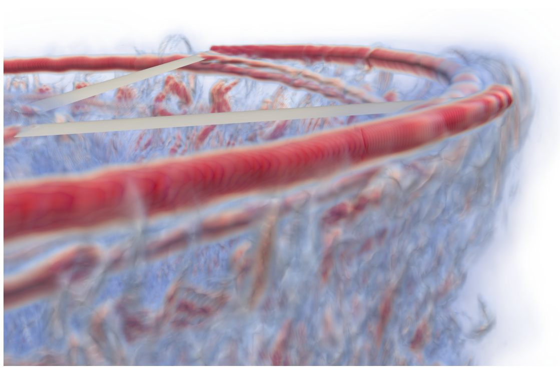

(e) $\frac{t-t_0}{\tau} = \frac{4}{24}$

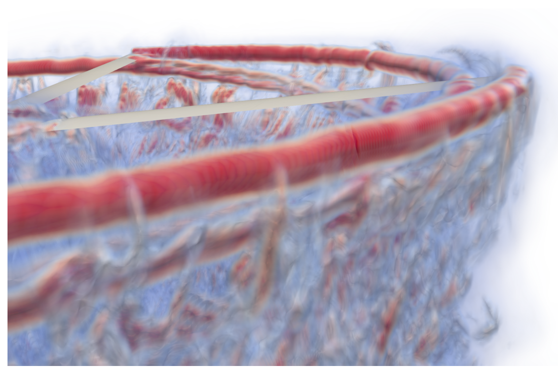

(f) $\frac{t-t_0}{\tau} = \frac{5}{24}$

Figure 11 Close-up visualization of the blade tip region of the S-76 rotor at $\theta_0 = 8^\circ$ (high resolution), at 6 successive instants over a quarter revolution (with τ the revolution period).

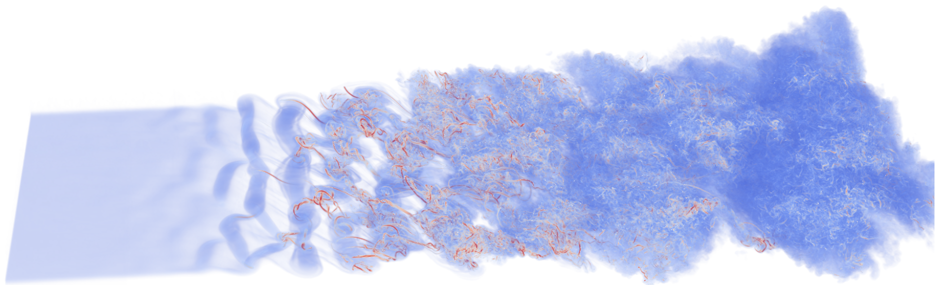

Figure 12 Spacial development of a shear layer with streamwise-aligned vorticity filaments forming between the main vortex rollers (results from [46])

Notice that the breakdowns observed in the wake of a hovering rotor are quite different from those of wind turbine wakes. In the latter case, the loss of coherence in the wake is mainly driven by the mutual-induction between successive tip vortices [47], effectively triggering a fundamental wake instability as predicted in [48]. Because of the global deceleration of the wake, the spacing between successive tip vortices decreases with the vortex age, thus increasing the amplification rate of the instabilities further into the wake. Hence, the breakdown generally occurs when the tip vortices are older than several rotor revolutions: the vortices start to pair or merge, which later gives rise to smaller vortical structures.

In the case of the hovering rotor, the spacing between successive tip vortices is relatively smaller due to the absence of an upstream velocity component. Furthermore, the wake accelerates, so the vortex spacing with the most unstable conditions is encountered right behind the rotor. While this proximity aggravates the mutual inductance, small scale instabilities are also excited through the presence of the secondary structures. Both types of instabilities can be observed in Fig. 11, eventually breaking the main vortices into smaller filaments, setting forth the conditions favorable to the transition to a fully turbulent flow. Hence, the conditions near the rotor are more instability-prone, and this might explain why the breakdown are generally observed after a vortex age corresponding to only one or two revolutions. Unfortunately, the lack of experimental data characterizing the breakdown of rotor-in-hover wakes currently prevents the establishment of clear conclusions about this phenomenon.

VII. Conclusions

In this paper, we studied the medium to large scale aerodynamics of helicopter rotors in hover by means of Large-Eddy Simulations performed using the Vortex Particle–Mesh method with Immersed Lifting Lines. The method was briefly presented. It solves the Navier-Stokes equations in their vorticity-velocity formulation, using a hybrid Lagrangian-Eulerian approach and sub-grid scales modeling. The ILL captures the effect of the blades on the fluid (akin to an actuator line model), but it maintains the Lagrangian character of the overall method —a key factor in the efficiency of this numerical method. The hovering scenarios of this work also rely on the novel FLUPS library to compute the velocity from the vorticity field, with truly unbounded boundary conditions on five of the six boundaries of the computational domain, and with an outflow condition on the sixth. Hence, we can simulate the rotors in tight domains (typically, a cube of edge length equal to $3R$) without affecting the free-space induction of the rotor. The associated computational cost is of the order of 2 600 CPU-hours for 20 rotor revolutions in our high resolution setup (192 particles per rotor diameter).

We evaluated the quality of the predictions of this approach against reference data, focussing on blade loadings, and on the vortex dynamics in the near-to-far wake. With the Knight and Hefner rotor, we demonstrated the suitability of our Poisson solver which is effectively procuring the free stream boundary conditions necessary for clean hover investigations. Generally, thrust coefficients are well predicted by the present method. However, too small torques lead to spurously high predictions of the figure of merit. An in-depth comparison of the loading on the S-76 blade revealed that four factors contribute to this inaccuracy:

1) the quality of the 2-D airfoil polars used in the Immersed Lifting Line;
2) the absence of a polar correction for 3-D effects in the root and tip regions;
3) the mollification of the line, leading to systematic underestimation of the torque at the tip;
4) the blade-vortex interaction occurring in the last 10% of the blade span.

While the first three limitations can be overcome with higher fidelity polar data and a specific treatment of the tip region regarding the effects of three-dimensionality and of mollification, the correct capture of the blade-vortex interaction by a lifting or an actuator line technique would require a specific correction to account for the possible effects of spanwise flow and local separation.

Nevertheless, despite the simplifications inherent to the ILL, the achieved level of accuracy are in line with those of the medium-fidelity simulation tools of the literature (purely Lagrangian methods, coupled approaches, or the VTM) while our method also provides a realistic unbounded flow boundary condition and a realistic description of the wake over large distances.

We showed that our simulation tool is capable of capturing most of the relevant physics associated with the near wake and its transition to a turbulent jet in the far field, at a fraction of the cost of blade-resolved CFDs. Even though the wake breakdown likely occurs too early in our simulations, our results on the S-76 rotor attested to the presence of secondary structures entangled between the primary tip vortices, as described in other experimental and numerical studies. From our observations, we traced back the origin of these structures in the blade vortex sheet being highly stretched between two successive tip vortices, supporting a hypothesis already exposed in the literature. We further hypothesized the role of these secondary structures in exciting the small-scale instabilities of the tip vortices, effectively accelerating the wake breakdown in a way dissimilar to what is generally observed in wind turbine wakes.

As a final note, we recall the disparities among the existing numerical studies on the phenomenon of wake breakdown in hovering rotors. Despite the numerous insights brought by several authors using various simulation tools, some underlying fundamental aspects behind these breakdowns remain unclear to date. Dedicated experimental results could help rule out what must be attributed to numerical artefacts in past studies, and identify the actual physics.

Acknowledgments

The authors acknowledge insightful discussions with Prof. Sven Schmitz (PennState University).

The development work benefited from the computational resources provided by the supercomputing facilities of the Université catholique de Louvain (CISM/UCL) and the Consortium des Équipements de Calcul Intensif (CÉCI) en Fédération Wallonie Bruxelles (FWB) funded by the Fond de la Recherche Scientifique de Belgique (F.R.S.-FNRS) under Convention No. 2.5020.11. The production simulations used computational resources made available on the Tier-1 supercomputer of the FWB, infrastructure funded by the Walloon Region under the Grant Agreement No. 1117545.

References

[1] Egolf, A., Hariharan, N. S., Narducci, R. P., and Reed, E., "AIAA Standardized Hover Simulation: Hover Performance Prediction Status and Outstanding Issues," *55th AIAA Aerospace Sciences Meeting*, 2017. https://doi.org/10.2514/6.2017-1429, URL https://arc.aiaa.org/doi/abs/10.2514/6.2017-1429.

[2] Komerath, N. M., Smith, M. J., and Tung, C., "A review of rotor wake physics and modeling," *Journal of the American Helicopter Society*, Vol. 56, No. 2, 2011, pp. 22006–22006. https://doi.org/10.4050/JAHS.56.022006.

[3] Kara, K., Brazell, M. J., Kirby, A. C., Mavriplis, D. J., and Duque, E. P., "Hover Predictions Using a High-Order Discontinuous Galerkin Off-Body Discretization," *AIAA Scitech 2020 Forum*, 2020. https://doi.org/10.2514/6.2020-0771, URL https://arc.aiaa.org/doi/abs/10.2514/6.2020-0771.

[4] Chaderjian, N. M., and Ahmad, J. U., "Detached eddy simulation of the UH-60 Rotor wake using adaptive mesh refinement," *American Helicopter Society 68th Annual Forum*, Texas, 2012.

[5] Jain, R., "Hover Predictions on the S-76 Rotor with Tip Shape Variation Using Helios," *Journal of Aircraft*, Vol. 55, No. 1, 2018, pp. 66–77. https://doi.org/10.2514/1.C034075, URL https://doi.org/10.2514/1.C034075.

[6] Forsythe, J. R., Lynch, E., Polsky, S., and Spalart, P., "Coupled flight simulator and CFD calculations of ship airwake using kestrel," *53rd AIAA Aerospace Sciences Meeting*, 2015, p. 0556. https://doi.org/10.2514/6.2015-0556.

[7] Stanly, R., Delorme, Y. T., and Frankel, S. H., "Computational Assessment of Actuator Line Model for Large Eddy Simulation of Rotor Noise," *AIAA Scitech 2020 Forum*, 2020. https://doi.org/10.2514/6.2020-0035, URL https://arc.aiaa.org/doi/abs/10.2514/6.2020-0035.

[8] Sorensen, J. N., and Shen, W. Z., "Numerical modeling of wind turbine wakes," *Journal of Fluids Engineering - Transactions of the ASME*, Vol. 124, No. 2, 2002, pp. 393–399. https://doi.org/10.1115/1.1471361.

[9] Martinez-Tossas, L. A., Churchfield, M. J., and Leonardi, S., “Large eddy simulations of the flow past wind turbines: actuator line and disk modeling,” *Wind Energy*, Vol. 18, No. 6, 2015, pp. 1047–1060. https://doi.org/doi.org/10.1002/we.1747.

[10] Churchfield, M. J., Schreck, S., Martinez-Tossas, L. A., Meneveau, C., and Spalart, P. R., “An Advanced Actuator Line Method for Wind Energy Applications and Beyond,” *35th Wind Energy Symposium*, AIAA, 2017, p. 1998. https://doi.org/doi.org/10.2514/6.2017-1998.

[11] Brown, R. E., and Line, A. J., “Efficient high-resolution wake modeling using the vorticity transport equation,” *AIAA journal*, Vol. 43, No. 7, 2005, pp. 1434–1443. https://doi.org/10.2514/1.13679.

[12] Whitehouse, G. R., Wachspress, D. A., and Quackenbush, T. R., “Predicting the Influence of Blade Shape on Hover Performance with Comprehensive Analyses,” *Journal of Aircraft*, Vol. 55, No. 1, 2018, pp. 111–121. https://doi.org/10.2514/1.C034073, URL https://doi.org/10.2514/1.C034073.

[13] Singh, P., and Friedmann, P. P., “Application of Vortex Methods to Coaxial Rotor Wake and Load Calculations in Hover,” *Journal of Aircraft*, Vol. 55, No. 1, 2018, pp. 373–381. https://doi.org/10.2514/1.C034520, URL https://doi.org/10.2514/1.C034520.

[14] Tan, J., Sun, Y., and Barakos, G., “Unsteady loads for coaxial rotors in forward flight computed using a vortex particle method,” *The Aeronautical Journal*, Vol. 122, No. 1251, 2018, pp. 693–714. https://doi.org/10.1017/aer.2018.8.

[15] He, C., and Rajmohan, N., “Modeling the Aerodynamic Interaction of Multiple Rotor Vehicles and Compound Rotorcraft with Viscous Vortex Particle Method,” *American Helicopter Society 72nd Annual Forum*, West Palm Beach, 2016.

[16] Shi, Y., Xu, G., and Wei, P., “Rotor wake and flow analysis using a coupled Eulerian–Lagrangian method,” *Engineering Applications of Computational Fluid Mechanics*, Vol. 10, No. 1, 2016, pp. 384–402. https://doi.org/10.1080/19942060.2016.1174887, URL https://doi.org/10.1080/19942060.2016.1174887.

[17] Wilbur, I. C., Moushegian, A., Smith, M. J., and Whitehouse, G. R., “UH-60A Rotor Analysis with an Accurate Dual-Formulation Hybrid Aeroelastic Methodology,” *Journal of Aircraft*, Vol. 57, No. 1, 2020, pp. 113–127. https://doi.org/10.2514/1.C035467, URL https://doi.org/10.2514/1.C035467.

[18] Chatelain, P., Backaert, S., Winckelmans, G., and Kern, S., “Large eddy simulation of wind turbine wakes,” *Flow, Turbulence and Combustion*, Vol. 91, No. 3, 2013, pp. 587–605. https://doi.org/10.1007/s10494-013-9474-8.

[19] Chatelain, P., Duponcheel, M., Caprace, D.-G., Marichal, Y., and Winckelmans, G., “Vortex particle-mesh simulations of vertical axis wind turbine flows: from the airfoil performance to the very far wake,” *Wind Energy Science*, Vol. 2, No. 1, 2017, p. 317. https://doi.org/10.5194/wes-2-317-2017.

[20] Chatelain, P., Duponcheel, M., Zeoli, S., Buffin, S., Caprace, D.-G., Winckelmans, G., and Bricteux, L., “Investigation of the effect of inflow turbulence on vertical axis wind turbine wakes,” *Journal of Physics: Conference Series*, Vol. 854, No. 1, 2017, p. 012011. https://doi.org/10.1088/1742-6596/854/1/012011.

[21] Caprace, D.-G., Chatelain, P., and Winckelmans, G., “Wakes of rotorcraft in advancing flight: A large eddy simulation study,” *Physics of Fluids*, Vol. 32, No. 8, 2020, p. 087107. https://doi.org/10.1063/5.0015162.

[22] Hariharan, N. S., “An Overview of Wake-Breakdown in High-Fidelity Simulations of Rotor in Hover,” *AIAA Scitech 2020 Forum*, 2020. https://doi.org/10.2514/6.2020-0530, URL https://arc.aiaa.org/doi/abs/10.2514/6.2020-0530.

[23] Knight, M., and Hefner, R. A., “Static thrust analysis of the lifting airscrew,” Tech. rep., NACA-TN-626, 1937.

[24] Cocle, R., Winckelmans, G., and Daeninck, G., “Combining the vortex-in-cell and parallel fast multipole methods for efficient domain decomposition simulations,” *Journal of Computational Physics*, Vol. 227, No. 21, 2008, pp. 9091–9120. https://doi.org/10.1016/j.jcp.2007.10.010.

[25] Cottet, G.-H., and Koumoutsakos, P., *Vortex Methods, Theory and Practice*, Cambridge University Press, 2000.

[26] Winckelmans, G. S., “Vortex Methods,” *Encyclopedia of Computational Mechanics*, Vol. 3, John Wiley & Sons, Ltd, 2004, 2$^{\text{nd}}$ ed., pp. 129–153. https://doi.org/10.1002/0470091355.ecm055.

[27] Chatelain, P., Curioni, A., Bergdorf, M., Rossinelli, D., Andreoni, W., and Koumoutsakos, P., “Billion vortex particle Direct Numerical Simulations of aircraft wakes,” *Computer Methods in Applied Mechanics and Engineering*, Vol. 197, No. 13, 2008, pp. 1296–1304. https://doi.org/10.1016/j.cma.2007.11.016.

[28] Sbalzarini, I. F., Walther, J. H., Bergdorf, M., Hieber, S. E., Kotsalis, E. M., and Koumoutsakos, P., "PPM A highly efficient parallel particle mesh library for the simulation of continuum systems," *J. Comput. Phys.*, Vol. 215, 2006, pp. 566–588. https://doi.org/10.1016/j.jcp.2005.11.017.

[29] Chatelain, P., and Koumoutsakos, P., "A Fourier-based elliptic solver for vortical flows with periodic and unbounded directions," *Journal of Computational Physics*, Vol. 229, No. 7, 2010, pp. 2425–2431. https://doi.org/10.1016/j.jcp.2009.12.035.

[30] Caprace, D.-G., Gillis, T., and Chatelain, P., "FLUPS - A Fourier-based Library of Unbounded Poisson Solvers," *SIAM Journal on Scientific Computing (forthcoming)*, 2021.

[31] Caprace, D.-G., Winckelmans, G., and Chatelain, P., "An immersed lifting and dragging line model for the vortex particle-mesh method," *Theoretical and Computational Fluid Dynamics*, Vol. 34, 2020, pp. 21–48. https://doi.org/10.1007/s00162-019-00510-1.

[32] Caprace, D.-G., Chatelain, P., and Winckelmans, G., "Lifting Line with Various Mollifications: Theory and Application to an Elliptical Wing," *AIAA Journal*, Vol. 57, No. 1, 2019, pp. 17–28. https://doi.org/10.2514/1.J057487.

[33] Meyer Forsting, A. R., Pirrung, G. R., and Ramos-García, N., "A vortex-based tip/smearing correction for the actuator line," *Wind Energy Science*, Vol. 4, No. 369-383, 2019. https://doi.org/10.5194/wes-2018-76.

[34] Angot, P., Bruneau, C., and Fabrie, P., "A penalization method to take into account obstacles in incompressible viscous flows," *Numerische Mathematik*, Vol. 81, 1999, pp. 497–520. https://doi.org/10.1007/s002110050401.

[35] Shives, M., and Crawford, C., "Mesh and load distribution requirements for actuator line CFD simulations," *Wind Energy*, Vol. 16, No. 8, 2013, pp. 1183–1196. https://doi.org/10.1002/we.1546.

[36] Pradeep, D. S., and Hussain, F., "Effects of boundary condition in numerical simulations of vortex dynamics," *Journal of Fluid Mechanics*, Vol. 516, 2004, pp. 115–124. https://doi.org/10.1017/S002211200400076X.

[37] Balch, D., and Lombardi, J., "Experimental study of main rotor tip geometry and tail rotor interactions in hover. Volume 1: Text and figures," Tech. Rep. CR-177336-VOL-1, NASA, 1985.

[38] Balch, D., and Lombardi, J., "Experimental study of main rotor tip geometry and tail rotor interactions in hover. Volume 2: Run log and tabulated data," Tech. Rep. CR-177336-VOL-2, NASA, 1985.

[39] Abras, J. N., and Hariharan, N., "Comparison of Computational Fluid Dynamics Hover Predictions on the S-76 Rotor," *Journal of Aircraft*, Vol. 55, No. 1, 2018, pp. 12–22. https://doi.org/10.2514/1.C034121, URL https://doi.org/10.2514/1.C034121.

[40] Drela, M., "XFOIL: An analysis and design system for low Reynolds number airfoils," *Low Reynolds number aerodynamics*, Vol. 54, Springer, 1989, pp. 1–12. https://doi.org/10.1007/978-3-642-84010-4_1.

[41] Garcia, A. J., and Barakos, G. N., "Hover Performance Predictions for the S-76 Main Rotor Blade," *53rd AIAA Aerospace Sciences Meeting*, 2015. https://doi.org/10.2514/6.2015-1712, URL https://arc.aiaa.org/doi/abs/10.2514/6.2015-1712.

[42] Garmann, D. J., and Visbal, M. R., "Interactions of a streamwise-oriented vortex with a finite wing," *Journal of Fluid Mechanics*, Vol. 767, 2015, pp. 782–810. https://doi.org/10.2514/6.2014-1282.

[43] Dag, K., and Sørensen, J. N., "A new tip correction for actuator line computations," *Wind Energy*, Vol. 23, No. 2, 2019, pp. 148–160. https://doi.org/10.1002/we.2419, URL https://onlinelibrary.wiley.com/doi/abs/10.1002/we.2419.

[44] Abras, J., Hariharan, N. S., and Narducci, R. P., "Wake Breakdown of High-fidelity Simulations of a Rotor in Hover," *AIAA Scitech 2019 Forum*, 2019. https://doi.org/10.2514/6.2019-0593, URL https://arc.aiaa.org/doi/abs/10.2514/6.2019-0593.

[45] Wolf, C. C., Schwarz, C., Kaufmann, K., Gardner, A. D., Michaelis, D., Bosbach, J., Schanz, D., and Schröder, A., "Experimental study of secondary vortex structures in a rotor wake," *Experiments in Fluids*, Vol. 60, No. 11, 2019, p. 175. https://doi.org/10.1007/s00348-019-2807-1, URL https://doi.org/10.1007/s00348-019-2807-1.

[46] Caprace, D.-G., Henneaux, D., Chatelain, P., and Winckelmans, G., "Video: Space Developing Shear Layer with Weak Inflow Turbulence," *70th Annual Meeting of the APS Division of Fluid Dynamics - Gallery of Fluid Motion*, American Physical Society, 2017. https://doi.org/10.1103/aps.dfd.2017.gfm.v0028, URL https://doi.org/10.1103/aps.dfd.2017.gfm.v0028.

[47] Marten, D., Paschereit, C. O., Huang, X., Meinke, M., Schröder, W., Müller, J., and Oberleithner, K., "Predicting Wind Turbine Wake Breakdown Using a Free Vortex Wake Code," *AIAA Journal*, Vol. 58, No. 11, 2020, pp. 4672–4685. https://doi.org/10.2514/1.J058308, URL https://doi.org/10.2514/1.J058308.

[48] Widnall, S. E., "Stability of a helical vortex filament," *J. Fluid. Mech.*, Vol. 54, No. 22, 1972, pp. 641–663. https://doi.org/10.1017/S0022112072000928.